Multi-band Bloch Equations and Gain Spectra of Highly Excited II-VI Semiconductor Quantum Wells

A. Girndt, F. Jahnke, A. Knorr, and S.W. Koch

Fachbereich Physik und Zentrum für Materialwissenschaften,

Phillips-Universität, Renthof 5, D-35032 Marburg, Germany

W.W. Chow

Sandia National Laboratories, Albuquerque, NM 87185-0601, U.S.A.

(April 21, 1997)

Abstract

Quasi-equilibrium excitation dependent optical probe spectra of II-VI semiconductor quantum wells at room temperature are investigated within the framework of multi-band semiconductor Bloch equations. The calculations include correlation effects beyond the Hartree-Fock level which describe dephasing, interband Coulomb correlations and band-gap renormalization in second Born approximation. In addition to the carrier-Coulomb interaction, the influence of carrier-phonon scattering and inhomogeneous broadening is considered. The explicit calculation of single particle properties like band structure and dipole matrix elements using $\mathbf{k} \cdot \mathbf{p}$ theory makes it possible to investigate various II-VI material combinations. Numerical results are presented for CdZnSe/ZnSe and CdZnSe/MgZnSSe semiconductor quantum-well systems.

Keywords: A. semiconductors B. optical properties C. carrier-carrier interaction

I. INTRODUCTION

Wide band gap semiconductor materials, in particular II-VI compounds, are promising candidates for optical device application in the blue-green wavelength region. Especially for device optimization, a detailed understanding of the electronic interaction processes and their influence on optical gain spectra is desirable. Several recently investigated II-VI heterostructures are composed of quantum layers with $Zn_xCd_{1-x}Se$ active material within ZnSe barriers [2–5]. Hence, the theoretical description of the optical properties of II-VI heterostructures requires not only the inclusion of the relevant many-body processes in a highly excited semiconductor but also the particular composition and geometry dependend band structure properties.

In this paper we theoretically investigate the optical probe spectra of II-VI heterostructures. Concentrating on room temperature properties of structures with weak interface roughness, the optical gain can be assumed to result from electrons which, after their incoherent injection, have relaxed into the available electronic states at the bottom of the band whereas higher bound states, such as biexcitons [6], are of minor importance. In our model, the interaction of the light field with the inverted material is treated semiclassically by calculating the absorption in the framework of the multi-band semiconductor Bloch equations. The observable in a typical experiment, where the probe light propagates in the plane of the quantum-well heterostructure, is the absorption coefficient,

$$\alpha(\omega) = \mu\Gamma\frac{\omega}{n_b}\,\mathrm{Im}\left[\frac{\tilde{P}(\omega)}{\tilde{E}(\omega)}\right], \tag{1}$$

where n_b the refractive index, $\tilde{E}(\omega) = \int dt\, e^{i\omega t}\, E(t)$ is the Fourier transform of the applied probe pulse $E(t)$ and $\tilde{P}(\omega)$ is the corresponding Fourier transform of the induced polarization density $P(t)$. Note that for a weak probe field the induced polarization $\tilde{P}(\omega)$ is directly proportional to $\tilde{E}(\omega)$ so that $\alpha(\omega)$ is independent of the probe-pulse parameters.

When light propagation in the quantum-well plane is experimentally investigated, the field overlapps with the quantum well(s) and the barrier layers. To account for the resulting

DISCLAIMER

reduced effective absorption or gain, we have introduced in Eq. (1) the confinement factor $\Gamma = 0.003/nm$.

II. EQUATIONS OF MOTION

In this section, we calculate the polarization density $P(t)$ from a microsocopic theory including band-structure effects as well as many body interactions. We expand the polarization density in a quantum-well Bloch basis,

$$P(t) = \frac{1}{A}\sum_{\nu,\nu'}\sum_{\mathbf{k}} \mu_{\mathbf{k}}^{\nu,\nu'} P_{\mathbf{k}}^{\nu,\nu'}(t) + \text{c.c.}, \tag{2}$$

where $\mathbf{k}$ is the in-plane carrier momentum, $\nu = \lambda, n$ contains the band index $\lambda = e, h$ and the sub-band index n and A is the active area of the quantum well. In Eq. (2), we consider all optically allowed single valence band to conduction band ($|\nu'\rangle \rightarrow |\nu\rangle$) transitions with the interband dipole matrix elements $\mu_{\mathbf{k}}^{\nu,\nu'}$. The polarizations for the different bands obey the multi-band semiconductor Bloch equations [7],

$$\frac{d}{dt}P_{\mathbf{k}}^{\nu,\nu'}(t) = -\frac{i}{\hbar}\Delta_{\mathbf{k}}^{\nu,\nu'} P_{\mathbf{k}}^{\nu,\nu'}(t) - \frac{i}{\hbar}\left[1 - f_{\mathbf{k}}^{\nu} - f_{\mathbf{k}}^{\nu'}\right]\Omega_{\mathbf{k}}^{\nu,\nu'}(t) + \left.\frac{dP_{\mathbf{k}}^{\nu,\nu'}(t)}{dt}\right|_{\text{corr}}, \tag{3}$$

where $P_{\mathbf{k}}^{\nu,\nu'}(t)$ is the interband polarization between the bands $\nu = e, n$ and $\nu' = h, n$ and $f_{\mathbf{k}}^{e,n}$, $f_{\mathbf{k}'}^{h,n}$ are the carrier distribution functions for electrons and holes in the sub-band n, respectively. For a weak probe beam, the polarization $P_{\mathbf{k}}^{\nu,\nu'}(t)$ remains linear with respect to the probe field $E(t)$ and the probe field induced changes of the carrier occupation $f_{\mathbf{k}}^{a,n}$ can be neglected. Hence the probe spectrum reflects the excitation of the system which is described by quasi-equilibrium Fermi-Dirac distribution functions $f_{\mathbf{k}}^{a,n}$ with fixed carrier temperature (T=300K) and a chemical potential determined by the total density in the sample.

In Eq. (2), the many-body effects can be devided into Hartee-Fock (mean field) and correlation contributions. The mean field corrections lead to renormalized single-particle energies,

$$\Delta_{\mathbf{k}}^{\nu,\nu'} = \epsilon_{\nu}(\mathbf{k}) - \epsilon_{\nu'}(\mathbf{k}) - \sum_{\mathbf{q}\neq\mathbf{k}} V_{|\mathbf{k}-\mathbf{q}|}\left(f_{\mathbf{q}}^{\nu} + f_{\mathbf{q}}^{\nu'}\right), \tag{4}$$

and to a renormalized Rabi energy,

$$\Omega_{\mathbf{k}}^{\nu,\nu'}(t) = \mu_{\mathbf{k}}^{\nu,\nu'} E(t) + \sum_{\mathbf{q}\neq\mathbf{k}} V_{|\mathbf{k}-\mathbf{q}|}\, P_{\mathbf{q}}^{\nu,\nu'}(t), \tag{5}$$

with the free-carrier energies $\epsilon_\nu(\mathbf{k})$ and the Rabi energy of the probe field $\mu_{\mathbf{k}}^{\nu,\nu'} E$. The particular properties of the heterostructure, such as quantum-well thickness and material composition, determine the dipole matrix transition elements $\mu_{\mathbf{k}}^{\nu,\nu'}$ as well as the bandstructure $\epsilon_\nu(\mathbf{k})$. In our approach, these quantities are calculated from a diagonalization of the Luttinger Hamiltonian using a 4×4 $\mathbf{k}\cdot\mathbf{p}$-theory within the envelope approximation [7].

The quantum-well matrix elements of the bare Coulomb potential, which couple various carrier states, have the general form

$$V^{\nu_1,\nu_2,\nu_3,\nu_4}(\mathbf{k}_1,\mathbf{k}_2,\mathbf{q}) = \frac{2\pi e^2}{\varepsilon_b\, q} \int dz\, dz' \tag{6}$$

$$\times\, \xi_{\nu_1}^*(\mathbf{k}_1,z)\, \xi_{\nu_2}^*(\mathbf{k}_2,z')\, e^{-q|z-z'|}\, \xi_{\nu_3}(\mathbf{k}_1+\mathbf{q},z')\, \xi_{\nu_4}(\mathbf{k}_2-\mathbf{q},z).$$

Because of the band mixing, the confinement functions $\xi_{\nu_i}(\mathbf{k}_i,z)$ of the band ν_i depend on the in-plane carrier momentum k_i. This band mixing is additionally complicated by the fact that the influence of barrier states on the top valence band states cannot be neglected. The dependence of the quantum-well Coulomb matrix elements on the band indices ν_i and the corresponding in-plane carrier momenta k_i considerably complicates the coupling of various bands in Eqs. (3)–(5) as well as the evaluation of screening. It would be desirable to use Eq. (6) without further approximations within the many-body problem. Then one would take into account that the Coulomb interaction explicitly depends on the momenta of the contributing carriers k_i and not only on the transition momentum q. In this paper, we study the influence of band mixing under the assumption that the various envelope functions $\xi_{\nu_i}(\mathbf{k}_i,z)$ in Eq. (6) are approximated by an effective (momentum independent) function $\xi_0(z)$. The resulting confinement Coulomb potential

$$V_q = \frac{2\pi e^2}{\varepsilon_b\, q} \int dz\, dz'\, |\xi_0(z)|^2\, e^{-q|z-z'|}\, |\xi_0(z')|^2 \tag{7}$$

will be used in Eqs. (4), (5) and below.

The mean-field contributions contain the lowest-order Coulomb effects which lead to excitonic resonances and a low-density band-gap renormalization. However, under high excitation conditions, correlation contributions [8–12] result in strong modifications of the Hartree-Fock terms. The correlation terms can be divided into diagonal (d) and non-diagonal (nd) contributions:

$$\left.\frac{dP^{\nu,\nu'}(\mathbf{k})}{dt}\right|_{\text{corr}} = -\left[\Gamma_{\text{d}}^{\nu}(\mathbf{k})+\Gamma_{\text{d}}^{\nu'}(\mathbf{k})\right]\, P^{\nu,\nu'}(\mathbf{k}) + \sum_{\mathbf{q}}\left[\Gamma_{\text{nd}}^{\nu}(\mathbf{k},\mathbf{q})+\Gamma_{\text{nd}}^{\nu'}(\mathbf{k},\mathbf{q})\right]\, P^{\nu,\nu'}(\mathbf{k}+\mathbf{q}). \tag{8}$$

The real part of Γ^{ν} describes the dephasing of the polarization due to scattering of carriers in the bands ν. The diagonal contribution, Re Γ_{d}^{ν}, leads to a momentum-dependent polarization decay rate whereas the non-diagonal contribution, Re Γ_{nd}^{ν}, mixes the polarizations of various k-states. Without higher-order polarization terms [9,12], which can be neglected in the regime where a weak probe field is treated, we find Re $\Gamma_{\text{d}}^{\nu}(\mathbf{k}) = \Sigma_{in}^{\nu}(\mathbf{k}) + \Sigma_{out}^{\nu}(\mathbf{k})$ where

$$\left.\frac{df^{\nu}(\mathbf{k})}{dt}\right|_{\text{corr}} = \Sigma_{in}^{\nu}(\mathbf{k})\,[1-f^{\nu}(\mathbf{k})] - \Sigma_{out}^{\nu}(\mathbf{k})\, f^{\nu}(\mathbf{k}) \tag{9}$$

determines the redistribution of the carrier occupation probability f^{ν}. Hence the diagonal damping rate contains the sum of in and out-scattering rates in the carrier dynamics. For the considered quasi-equilibrium situation of the carrier system, the detailed balance condition leads to $\frac{d}{dt}f^{\nu}(\mathbf{k})|_{\text{corr}}=0$ whereas in and out-scattering results in a large damping rate Re Γ_{d} which corresponds to a decay time on the order of 100 fs. In Eq. (8), this diagonal damping rate is compensated to a large extend by the non-diagonal damping rate Re Γ_{nd}. In Ref. [10] it has been shown, that this compensation has to be considered in order to obtain the correct carrier generation rate for intense optical interband excitation. Also the excitonic damping [14] and the lineshape of the gain [11] can be properly described only by including both diagonal and non-diagonal damping.

On the other hand, the imaginary part of Γ^{ν} combines with the mean-field contributions, described by Eqs. (4) and (5), by adding screening contributions to the renormalized carrier energy and and the renormalized Rabi energy. Note, however, that in general the correlation

contributions cannot be written as corrections to single particle properties.

In the following we consider the influence of carrier-carrier Coulomb scattering as well as carrier-phonon scattering. In second Born approximation, where terms up to the quadratic order in the screened Coulomb potential are included, the carrier-carrier scattering leads to the diagonal contribution

$$\Gamma_{\rm d}^{\nu(cc)}(\mathbf{k}) = \frac{1}{\hbar}\sum_{\mathbf{k}',\mathbf{q}}\sum_{\nu'}\left(2|W_{\mathbf{q}}|^2 - \delta_{\nu,\nu'}W_{\mathbf{q}}\,W_{\mathbf{k}+\mathbf{q}-\mathbf{k}'}\right)\,g(\epsilon_{\mathbf{k}}^{\nu}-\epsilon_{\mathbf{k}+\mathbf{q}}^{\nu}+\epsilon_{\mathbf{k}'}^{\nu'}-\epsilon_{\mathbf{k}'-\mathbf{q}}^{\nu'}) \times\left[f_{\mathbf{k}+\mathbf{q}}^{\nu}\left(1-f_{\mathbf{k}'}^{\nu'}\right)\,f_{\mathbf{k}'-\mathbf{q}}^{\nu'}+\left(1-f_{\mathbf{k}+\mathbf{q}}^{\nu}\right)\,f_{\mathbf{k}'}^{\nu'}\,\left(1-f_{\mathbf{k}'-\mathbf{q}}^{\nu'}\right)\right], \tag{10}$$

whereas the non-diagonal scattering rate follows from

$$\Gamma_{\rm nd}^{\nu(cc)}(\mathbf{k},\mathbf{q}) = \frac{1}{\hbar}\sum_{\mathbf{k}'}\sum_{\nu'}\left(2|W_{\mathbf{q}}|^2 - \delta_{\nu,\nu'}W_{\mathbf{q}}\,W_{\mathbf{k}+\mathbf{q}-\mathbf{k}'}\right)\,g(-\epsilon_{\mathbf{k}}^{\nu}+\epsilon_{\mathbf{k}+\mathbf{q}}^{\nu}-\epsilon_{\mathbf{k}'}^{\nu'}+\epsilon_{\mathbf{k}'-\mathbf{q}}^{\nu'}) \times\left[f_{\mathbf{k}}^{\nu}\,f_{\mathbf{k}'}^{\nu'}\,(1-f_{\mathbf{k}'-\mathbf{q}}^{\nu'})\;+\;(1-f_{\mathbf{k}}^{\nu})\,(1-f_{\mathbf{k}'}^{\nu'})\,f_{\mathbf{k}'-\mathbf{q}}^{\nu'}\right]. \tag{11}$$

In the subband matrix element of the screened 2d-Coulomb potential, $W_{\mathbf{q}} = V_{\mathbf{q}}/\epsilon_{\mathbf{q}}$, the influence of excitation-induced screening is described by the dielectric function $\epsilon_{\mathbf{q}}$ which will be calculated using the static Lindhard formula [13]. Screening contributions of the crystal lattice (including phonons) and nonresonant transitions are included through a background dielectric constant ϵ_b in Eq. (7). With $\epsilon_b = \epsilon_0$ background contributions of phonons are taken into account. However, as part of the phonons and their interaction with the carriers will be treated explicitly, this dielectric constant has to be reduced [13]. Hence, when we consider correlation contributions due to carrier-phonon interaction, we use a background dielectric constant $\epsilon_b = \epsilon_\infty$ which does not include the influence of phonons. In this limiting case, the background phonon screening is slightly underestimated.

For the electron-phonon scattering, the diagonal rates in Eq. (8) are given by

$$\Gamma_{\rm d}^{\nu(ph)}(\mathbf{k}) = \frac{1}{\hbar}\sum_{\mathbf{q}}\gamma_{\mathbf{q}}^2\left\{\left[(1-f_{\mathbf{k}-\mathbf{q}}^{\nu})\,n_{LO}\;+\;f_{\mathbf{k}-\mathbf{q}}^{\nu}\,(1+n_{LO})\right]\,g(\epsilon_{\mathbf{k}}^{\nu}-\epsilon_{\mathbf{k}-\mathbf{q}}^{\nu}+\hbar\omega_{LO}) + \left[(1-f_{\mathbf{k}-\mathbf{q}}^{\nu})\,(1+n_{LO})\;+\;f_{\mathbf{k}-\mathbf{q}}^{\nu}\,n_{LO}\right]\,g(\epsilon_{\mathbf{k}}^{\nu}-\epsilon_{\mathbf{k}-\mathbf{q}}^{\nu}-\hbar\omega_{LO})\right\}, \tag{12}$$

and the non-diagonal rates are

$$\Gamma_{\rm nd}^{\nu(ph)}(\mathbf{k},\mathbf{q}) = \frac{1}{\hbar}\sum_{a=\nu,\nu'} \gamma_{\mathbf{q}}^2 \Big\{ [(1-f_{\mathbf{k}}^a)\, n_{LO} + f_{\mathbf{k}}^a\,(1+n_{LO})]\; g(\epsilon_{\mathbf{k}-\mathbf{q}}^a - \epsilon_{\mathbf{k}}^a + \hbar\omega_{LO}) + [(1-f_{\mathbf{k}}^a)\,(1+n_{LO}) + f_{\mathbf{k}}^a\, n_{LO}]\; g(\epsilon_{\mathbf{k}-\mathbf{q}}^a - \epsilon_{\mathbf{k}}^a - \hbar\omega_{LO}) \Big\}, \qquad (13)$$

where $\hbar\omega_{\rm LO}$ is the energy of the LO-phonons and $\gamma_{\mathbf{q}}^2$ is the Fröhlich interaction matrix element of 3d LO-phonons and confined electrons with in-plane momentum $\mathbf{q}$,

$$\gamma_{\mathbf{q}}^2 = \int dq_z \, \frac{e^2}{4\pi\varepsilon_0\,\epsilon_{(|\mathbf{q}|^2+q_z^2)}\,(|\mathbf{q}|^2+q_z^2)} \left(\frac{1}{\epsilon_\infty} - \frac{1}{\epsilon_0}\right) \frac{\hbar\omega_{\rm LO}}{2}. \qquad (14)$$

For the distribution function of phonons, n_{LO}, we use a Bose-Einstein function containing the lattice temperature.

The derivation of the scattering rates requires many body techniques such as Green's functions or projection formalism in density matrix theory. Here, within the assumption that gain spectra at room temperature can be described by using one-particle correlations, higher order correlation functions have been factorized. In the Green's functions technique, the random-phase approximation (RPA) as well as the first Coulomb vertex contribution have to be considered to obtain all scattering contributions in Eqs. (10) and (11) which are quadratic in the screened Coulomb potential W. Correlation contributions have a complicated time dependence, which includes memory effects. In Eqs. (10) – (13), this time-dependence has been approximated within an adiabatic treatment that leads to a generalized Heitler-Zeta function,

$$g(\epsilon) = \frac{i}{\epsilon + i\gamma}. \qquad (15)$$

This Heitler-Zeta function includes the effective quasi-particle broadening γ which will be treated as a small constant. While γ is a property of correlated carriers, we do not include any phenomenolagical polarization decay time.

At the end of this section, we outline some properties of the discussed theory for a 4 nm CdZnSe quantum well (see next section). The dependence of our results on the effective quasi-particle broadening γ is shown in Fig. 1 where, for simplicity, only a single valence band has been considered. While the diagonal scattering rate is reduced with increasing

γ, the compensation of diagonal and non-diagonal rates results in a spectrum which is basically independent on γ. In Fig. 2 we study the influence of various approximations for the polarization dephasing on the absorption spectrum. In the simplest approximation, correlation contributions in Eq. (2) are included phenomenologically. Polarization dephasing, which is described by the real part of Eq. (8), has often been approximated by a constant T_2 time. Screening corrections to the Hartree-Fock terms, Eqs. (4) and (5), which follow from the imaginary part of Eq. (8), have been approximated by replacing V by W and adding the Coulomb-hole term in Eq. (4) [13]. The resulting absorption spectra are shown in Fig. 2a. With increasing carrier density, we obtain a strong artificial red shift of the exciton resonance (at moderate densities) and of the gain peak (at high densities). As a next step, we consider correlation contributions due to carrier-carrier scattering. In Fig. 2b, only the complex diagonal rate $\Gamma_{\mathrm{d}}^{\nu(cc)}(\mathbf{k})$ has been used together with Eqs. (4)–(8), whereas in Fig. 2c also the non-diagonal rate $\Gamma_{\mathrm{nd}}^{\nu(cc)}(\mathbf{k},\mathbf{q})$ has been included. When only the diagonal rate is considered, dephasing is clearly overestimated which can be seen from the strong broadening of the exciton resonances. Only if both diagonal and non-diagonal rates are included, the exciton broadening is reduced to reasonable values and, in agreement with experimental observations, almost no shift of the exciton resonance is obtained with increasing carrier density. In Figs. 2d and e, we directly compare the approximations of Figs. 2a-c for carrier densities leading to gain. In the phenomenological model (dotted line) as well as in the pure dephasing limit (dashed line), the bandgap renormalization is drastically overestimated, the lineshape of the gain is modified and unphysical absorption below the renormalized bandedge is obtained in comparison to the full model (solid line). Especially the absorption energetically below the gain region, which occurs in simplified gain calculations, is a signature of overestimated dephasing and incorrect lineshape. The resulting strong broadening of carrier lineshape functions leads to an unphysical admixture of non-inverted states high above the band edge.

In conclusion, the large red shift of the exciton at low carrier densities, the overestimated band-gap shift at higher densities as well as the large damping are artifacts of simpler

models which are in clear contradiction to experimental results. Hence, a pure dephasing approximation is not appropriate and only the full model can reproduce the experimental results.

For a realistic description of quantum wells on the basis of II-VI compounds, additional excitation independent inhomogeneous broadening has to be considered in addition to the excitation dependent carrier-carrier and carrier-phonon interaction. In particular, small spatial variations of the concentration of the quantum-well and barrier materials as well as roughness of the well/barrier interfaces give rise to inhomogenous broadening. Correspondingly the calculated results are more realistic when the homogeneously broadened spectrum $\alpha_{hom}(\omega)$ is convoluted with a Gaussian distribution $\mathcal{G}(\omega)$ of given spectral width according to

$$\alpha_{inh}(\omega) = \int d\omega' \, \alpha_{hom}(\omega - \omega') \, \mathcal{G}(\omega'). \tag{16}$$

Figure 3 shows the influence of increasing additional inhomogenous broadening on the TE-spectrum of a 4 nm CdZnSe quantum well (see next section). Note that the influence of inhomogeneous broadening is stronger for smaller carrier densities where the spectrum contains sharp features. With increasing broadening, the lineshape is modified and the gain maxima can shift several meV. In the following results, we have included an inhomogenous broadening of 10 meV.

III. SPECTRA OF II-VI QUANTUM WELLS

The microscopic model discussed in the previous section will be used to compute the density-dependent absorption and gain spectra for CdZnSe quantum wells between 15nm ZnSe barriers and ZnSSe cladding layers (25% Cd and 6% S). Two samples with a quantum-well width w=4 nm (QW1) and w=7 nm (QW2) are compared.

Using the envelope approximation method [7], the energy gaps and the strain induced shifts for the heavy and light hole states are calculated. The conduction bands are always

assumed to be parabolic. Neglecting the split off band, the hole states are coupled via a 4×4 Luttinger Hamiltonian. The diagonalization of this system leads to the valence bands $\epsilon_{\nu'}(\mathbf{k})$ and the dipol matrix elements $\mu_{\mathbf{k}}^{\nu,\nu'}$. All those bands are considered where the carriers are confined in the quantum well for at least small wavevectors $\mathbf{k}$. For the 4 nm and 7 nm quantum wells, the calculated band structure is shown in Fig. 4. In the 4 nm (7 nm) quantum well, one (two) conductions band and three (five) valence bands are confined. The compressive strain of the CdZnSe wells between the ZnSe barriers produces a heavy-hole light-hole splitting. For the 7 nm quantum well, the top three valence bands are heavy-hole like close to the band edge so that their coupling to the TM-mode is weak. Hence the exciton and gain corresponding to these transitions is small. The main contribution to the TM-mode follows from tansitions between the fourth and fifth valence band and the first conduction band.

The TE- and TM-spectra of the 4 nm and 7 nm quantum wells are plotted in Figs. 5 and 6, respectively. The shown carrier densities cover the region from no inversion between any bands to inversion between most of the confined bands for small wavevectors $\mathbf{k}$ [16].

The low-density TE-spectra of the 4 nm quantum well (left part in Fig. 5) show two strong excitonic absorption lines corresponding to the 1-1 and 2-2 transition. Here transitions are labeled i-j with i (j) refering to the conduction (valence) band involved. For our system, the second TE-absorption (2-2) line appears at the same spectral position as the TM-absorption (1-4) line; the differences of the band gaps for these transitions is less than 2meV. These excitonic absorption lines stay at their spectral position when the carrier density increases; after exciton bleaching the transition develops gain. For the highest carrier density, the TE-spectra of the 4 nm quantum well exhibit a shoulder due to inversion of the 2-2 transition. In addition, the left part of Fig. 5 shows that the absorption above the renormalized band edge does not decrease when the carrier density increases; the high-energy part of the spectra for large carrier densities is only shifted as a consequence of bandgap renormalization due to Coulomb interaction.

If the quantum well is wider, more bands are confined. This is illustrated in the right

part of Figs. 5 and 6. Due to the second conduction band in QW2, we obtain an additional excitonic transition in the TE-spectra while the TM-absorption remains similar to that of QW1. As the carrier density is distributed over more bands in QW2, the inversion becomes smaller and the gain is reduced. In addition, the polarization decay is increased for QW2 at low plasma densities which leads to a broader excitonic absorption line.

The band offset, i.e., the splitting of the confinement energy between the conduction and the valence band, cannot be determined unambiguously from experiments. In the previous calculations, a band offset of 60% for the conduction band has been assumed. The influence of band offset changes on our results is studied in Figs. 7 and 8 for the TE- and TM-spectra, respectively. For a conduction band offset between 30% and 60%, a single sub-band appears in the finite-hight quantum well confinement potential of the electrons using the above discussed material composition and 4 nm well width (QW1). However, the confinement potential of holes leads to four sub-bands within the quantum well for 30% and 40% offset and three sub-bands when 50% and 60% offset are considered. The TE-spectra for various band-offset values are shown in Fig. 7. The lineshape of the spectra at high densities is almost independent of the band offset; only the magnitude of the gain is slightly changed. Also the low-density spectra are similar, only the weak excitonic resonance of the fourth hole subband is missing for a band offset $\geq 50\%$. With increasing band offset, the envelope function of the light hole becomes less confined in the quantum well which leads to an reduced effective TM-dipol coupling with the conduction band. For that reason both the TM-absorption for low plasma densities and TM-gain at higher densities are reduced with increasing band offset as shown in Fig. 8.

As another application of our theory, we study the influence of compressive versus tensile strain on the quantum-well spectra of II-VI compounds. We investigate a 4 nm $Zn_{0.8}Cd_{0.2}Se$ quantum well with a lattice constant of 5.75 Å between ZnMgSSe barriers having a lattice constant of either 5.65 Å (QW3) or 5.83 Å (QW4) [17]. The corresponding band structure is shown in Fig. 9. In QW3, the first three valence bands are heavy-hole like at the zone center while in QW4 the tensile strain causes a top valence band with light-hole character.

Therefore, the TE-gain strongly exceeds the TM-gain for compressive strain whereas for tensile strain the TM-gain is dominant (Fig. 10). The carrier density dependence of the TE-spectrum for QW3 is shown in Fig. 11. At intermediate densities, a situation can be realized where a small gain exists while the excitonic enhancement is still present. A similar situation has recently been observed in ZnCdSe/ZnSSe/ZnMgSSe quantum wells [18].

IV. CONCLUSION

In summary, the gain spectra of II-VI quantum-well materials have been investigated within a microscopic plasma theory which is based on kinetic equations for an interacting electron-hole system in a multi-band semiconductor. These equations include many-body effects such as intraband as well as interband Coulomb correlations leading to carrier scattering and excitonic transitions. In addition, the influence of LO-phonons has been considered. The single-particle energies and the dipole coupling have computed using Luttinger-Kohn theory in envelope function approximation.

The model has been used for calculating the excitation density dependent absorption and gain spectra of several different examples. The possibility to optimize the gain spectra in terms of well-width and composition has been studied for II-VI compounds.

This work was supported by the Deutsche Forschungsgemeinschaft through the "Schwerpunktprogramm II-VI-Halbleiterstrukturen", the Leibniz prize, the AFOSR grant 49620-97-1-0002, and the DOE contract DE-AC04-94AL85000. We acknowledge valuable discussions with J. Moloney and coworkers, and a grant for CPU time at the Forschungszentrum Jülich.

REFERENCES

[1]

[2] M.A. Haase, J. Qui, J.M. De Puydt, and H. Cheng, Appl. Phys. Lett. **59** , 1272 (1991).

[3] A.V. Nurmikko, R.L. Gunshor, and M. Kobazyashi, J. Vac. Sci. Technol B **10**, 2056 (1992).

[4] See e.g. contributions to *Proceedings of the International Workshop on ZnSe-Based Blue-Green Laser Structures, 1994*, [Phys. Status Solidi B **187** (1995)].

[5] W.W. Chow, and S.W. Koch, Appl. Phys. Lett. **66** (22), 3004 (1995).

[6] F. Kreller, M. Lowitsch, J. Puls, and F. Henneberger, Phys. Rev. Lett. **75**, 2420 (1995).

[7] For a textbook discussion see, W.W. Chow, S.W. Koch, and M. Sargent. III, *Semiconductor-Laser Physics* (Springer, Berlin, 1994).

[8] M. Lindberg and S.W. Koch, Phys. Rev. **B 38**, 3342 (1988).

[9] T. Rappen, U.G. Peter, M. Wegener, and W. Schäfer, Phys. Rev. **B 49**, 10 774 (1994).

[10] F. Rossi and S. Haas and T. Kuhn, Phys. Rev. Lett. **72**, 152 (1994).

[11] A. Knorr, S. Hughes, T. Stroucken, S.W. Koch, Chem. Phys. **210**, 27 (1996).

[12] F. Jahnke, M. Kira and S.W. Koch, "Linear and Nonlinear Optical Properties of Quantum Confined Excitons in Semiconductor Microcavities", Phys. Rev. B., submitted.

[13] For a textbook discussion see, H. Haug and S.W. Koch, *Quantum Theory of the Optical and Electronic Properties of Semiconductors*, World Scientific, Singapore, 3rd ed., (1994).

[14] F. Jahnke, M. Kira, S.W. Koch, G. Khitrova, E.K. Lindmark, T.R. Nelson Jr., D.V. Wick, J.D. Berger, O. Lyngnes, H.M. Gibbs and K. Tai, Phys. Rev. Lett. **77**, 5257 (1996).

[15] S.Hughes, A.Knorr, S.W.Koch, R.Binder, R.Indik, and J.Moloney, Solid State Comm. **100**, 555 (1996).

[16] For the inversion at the band edge $I^{\nu,\nu'} = f^{\nu}(\mathrm{k}=0) + f^{\nu'}(\mathrm{k}=0) - 1$ we obtain with the lowest carrier density $n = 0.5 \times 10^{12}$ cm^{-2}: $I^{1,1} = -0.63$, $I^{2,5} = -0.98$ and with the highest density $n = 8.0 \times 10^{12}$ cm^{-2}: $I^{1,1} = +0.79$, $I^{1,5} = +0.69$, $I^{2,1} = +0.50$, $I^{2,3} = +0.12$, $I^{2,4} = -0.22$, $I^{2,5} = -0.22$.

[17] W. Huang and F.C Jain Appl. Phys. Lett. **66**, 1596 (1995).

[18] J. Ding, V. Kozlov, P. Kelkar, A. Salokatve, and A.V. Nurmikko, phys. stat. sol. (b) **188**, 153 (1995).

FIGURES

FIG. 1. Complex scattering rate $\Gamma_d^{\nu(cc)}(\mathbf{k})$ for electrons (e) and holes (h) and absorption spectrum for a two-band model with carrier density 2×10^{12} cm^{-2} and various quasi-particle broadening γ.

FIG. 2. Influence of the polarization-dephasing model on the linear absorption spectrum of a 4 nm CdZnSe quantum well. Within a phenomenological model (a), a constant polarization decay rate T_2=100 fs and screened Hartree-Fock contributions have been considered. Using a microscopic model for correlation contributions due to carrier-carrier scattering, we compare the diagonal dephasing (b) with diagonal *and* non-diagonal dephasing (c). The carrier densities are 0.1, 0.5, 1, 2, 4 $\times 10^{12}$ cm^{-2} (from top to bottom). In (d) and (e) we directly compare the phenomenological model (dotted line) with the diagonal dephasing (dashed line) and diagonal + non-diagonal dephasing (solid line) for a fixed carrier density.

FIG. 3. Absorption spectrum of a 4 nm quantum well for a carrier density 2×10^{12} cm^{-2} and various inhomogeneous broadening.

FIG. 4. Energy bands for a 4 nm and 7 nm CdZnSe/ZnSe quantum well. The offset energy E_1 is 2.52 eV.

FIG. 5. Comparison of the TE-spectra of a CdZnSe/ZnSe quantum well with 4 nm well width (QW1) and 7 nm well width (QW2). The carrier densities are 0.5, 1, 2, 3, 4, 5, 6, 7, 8×10^{12} cm^{-2} (from top to bottom). An additional inhomogenous broadening of 10 meV is taken into account. The bottom figures show the same on a larger scale.

FIG. 6. Same as Fig. 5 for the TM-spectra.

FIG. 7. TE-spectra for QW1 where different band offsets are assumed. The densities are similar as in Fig.(6). For 30% or 40% conduction-band offset, four valence bands are confined in the well and three valence bands for higher offsets.

FIG. 8. Same as Fig. 7 for the TM-spectra. By increasing the conduction-band offset, i.e., reducing the potential well for the holes, the light hole becomes less confined and therefore the TM-coupling of the conduction bands with the confined valence bands decreases.

FIG. 9. Energy bands for a 4 nm CdZnSe/ZnMgSSe quantum well with compressive (QW3) and tensile (QW4) strain. The offset energy E_2 is 2.68 eV.

FIG. 10. TE- and TM-spectra for a 4 nm CdZnSe/ZnMgSSe quantum well with compressive (QW3) and tensile (QW4) strain at carrier density 6 $\times 10^{12}$ cm^{-2}. The bottom figures show the same on a larger scale.

FIG. 11. TE-spectra for a 4 nm CdZnSe/ZnMgSSe quantum well with compressive strain (QW3) for carrier densities 1.5, 1.8, 2.0, 2.2, 2.5 and 4.0 $\times 10^{12}$ cm^{-2} (from top to bottom). The bottom figure shows the same on a larger scale.

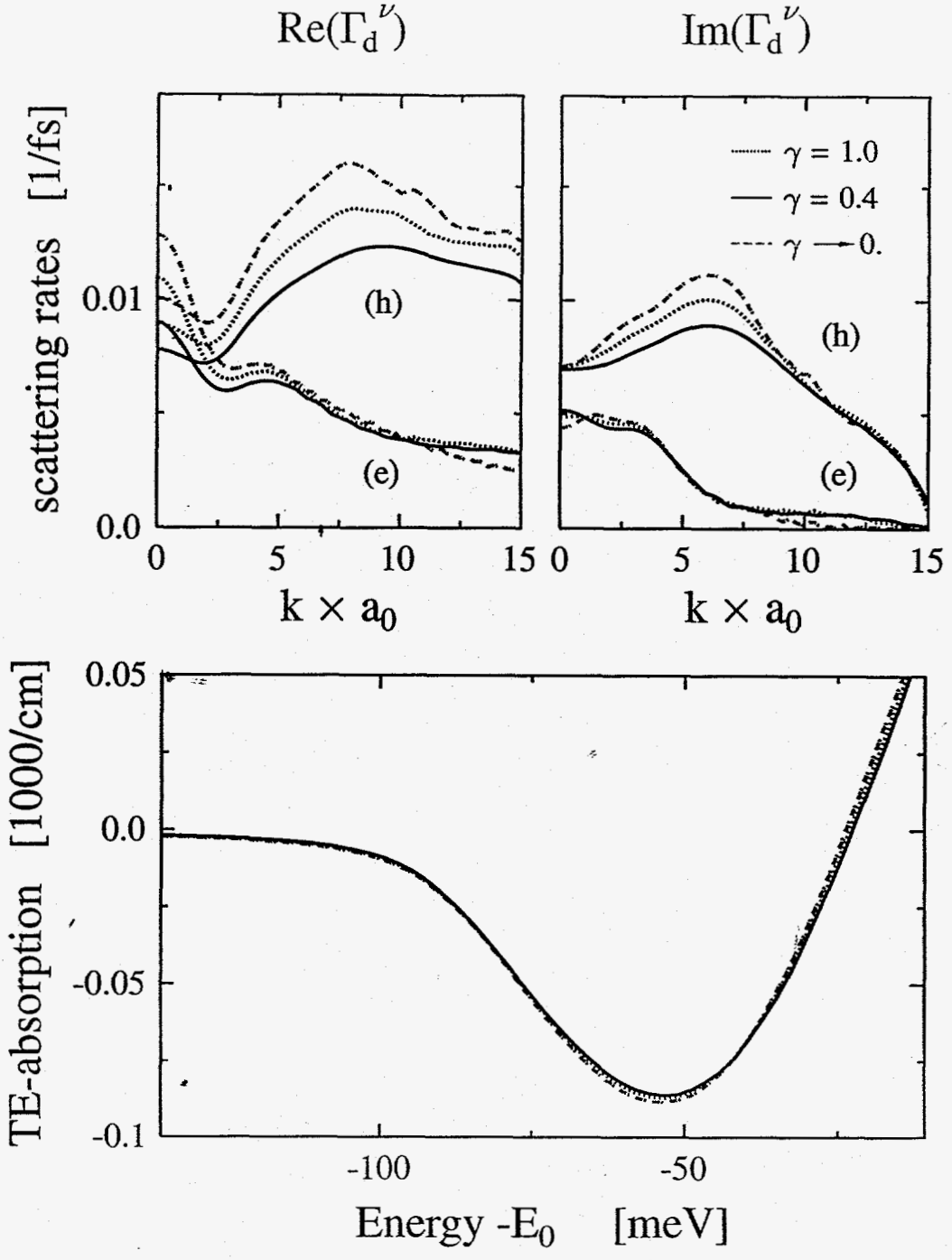
Re(Γ_d^ν)
Im(Γ_d^ν)
scattering rates [1/fs]
0.01
0.0
(h)
(e)
γ = 1.0
γ = 0.4
$\gamma \to$ 0.
0
5
10
15
k × a_0
TE-absorption [1000/cm]
0.05
0.0
-0.05
-0.1
-100
-50
Energy -E_0 [meV]

Fig 1

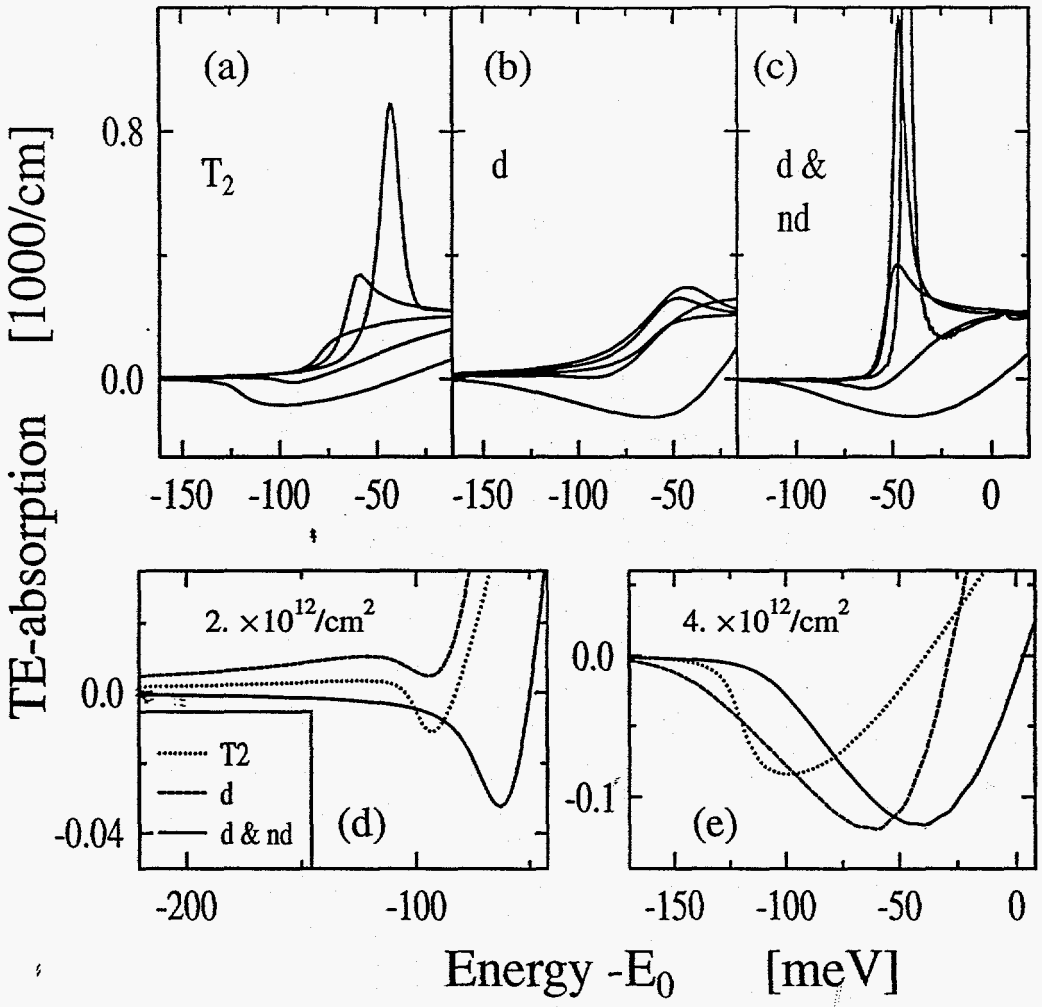
(a)
(b)
(c)
T_2
d
d &
nd
0.8
0.0
-150 -100 -50
-150 -100 -50
-100 -50 0
TE-absorption [1000/cm]
2. $\times 10^{12}$/cm^2
4. $\times 10^{12}$/cm^2
0.0
-0.04
0.0
-0.1
T2
d
d & nd
(d)
(e)
-200 -100
-150 -100 -50 0
Energy -E_0 [meV]

Fig 2

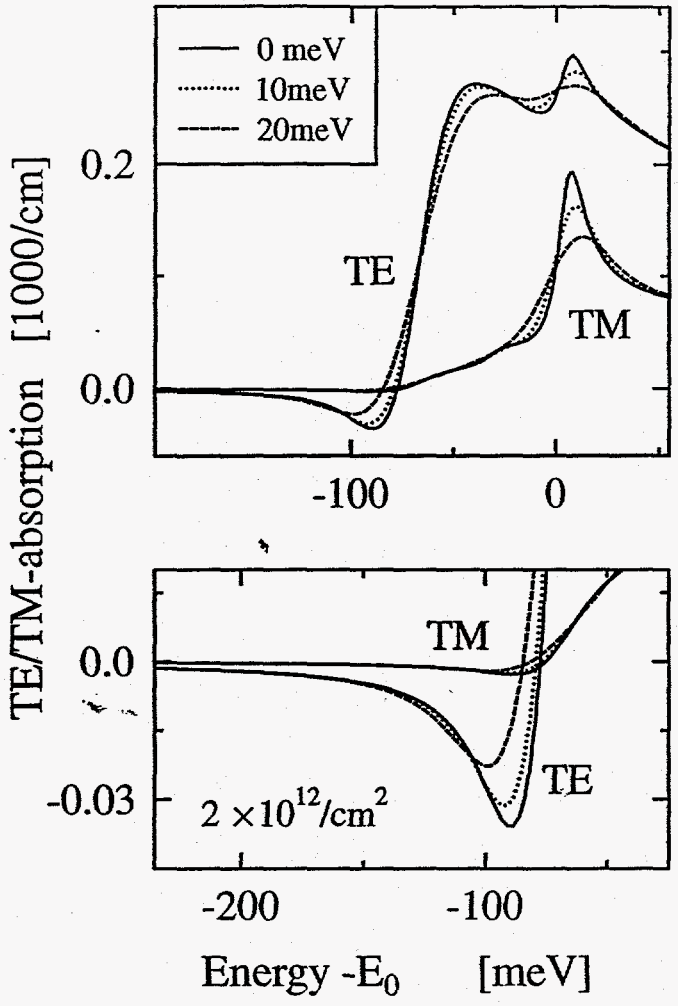
0 meV
10meV
20meV
0.2
0.0
TE
TM
-100
0
TM
0.0
-0.03
TE
2 ×10^12/cm^2
-200
-100
TE/TM-absorption [1000/cm]
Energy -E0 [meV]

Fig 3

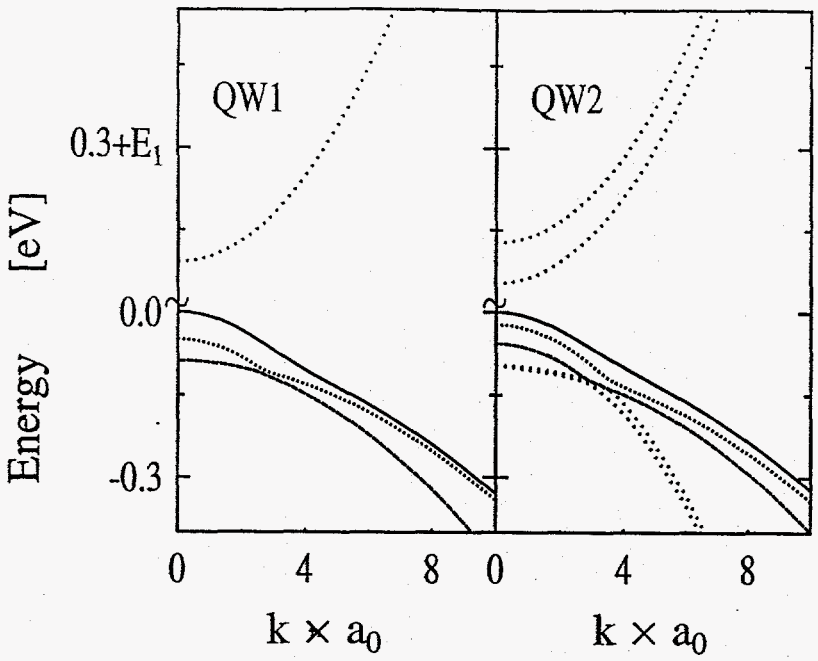

Fig 4

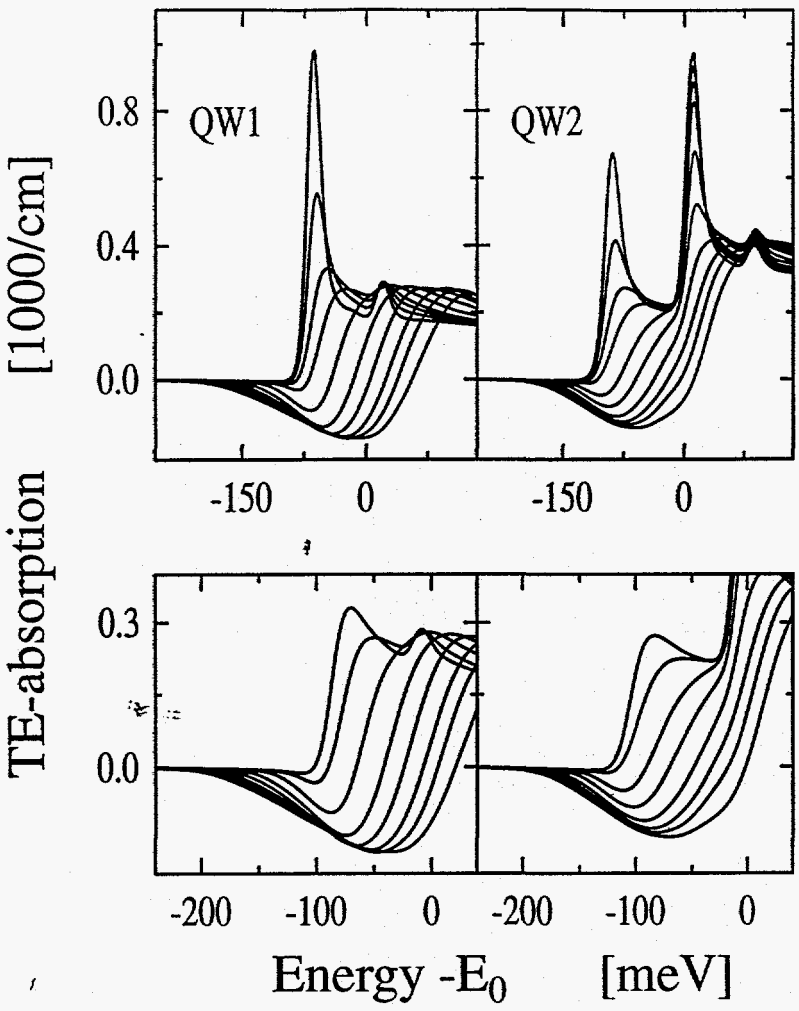
QW1
QW2
0.8
0.4
0.0
-150
0
0.3
0.0
-200
-100
0
TE-absorption [1000/cm]
Energy -E0 [meV]

Fig 5

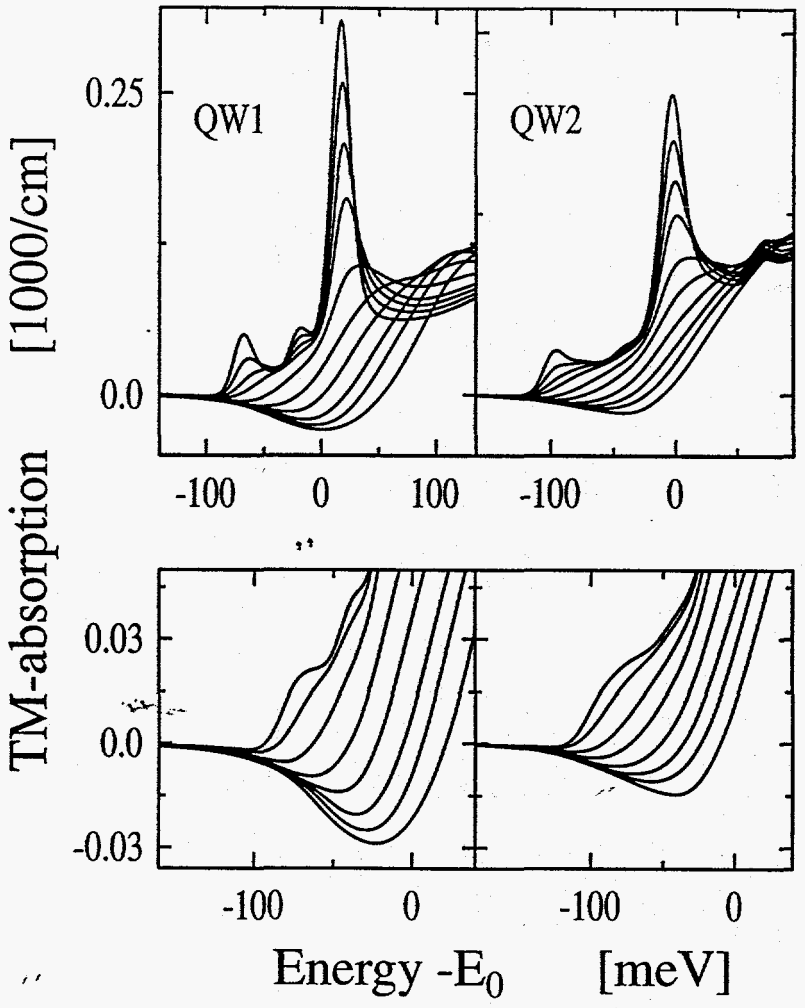
QW1
QW2
0.25
0.0
-100
0
100
-100
0
0.03
0.0
-0.03
-100
0
-100
0
TM-absorption [1000/cm]
Energy -E0 [meV]

Fig 6

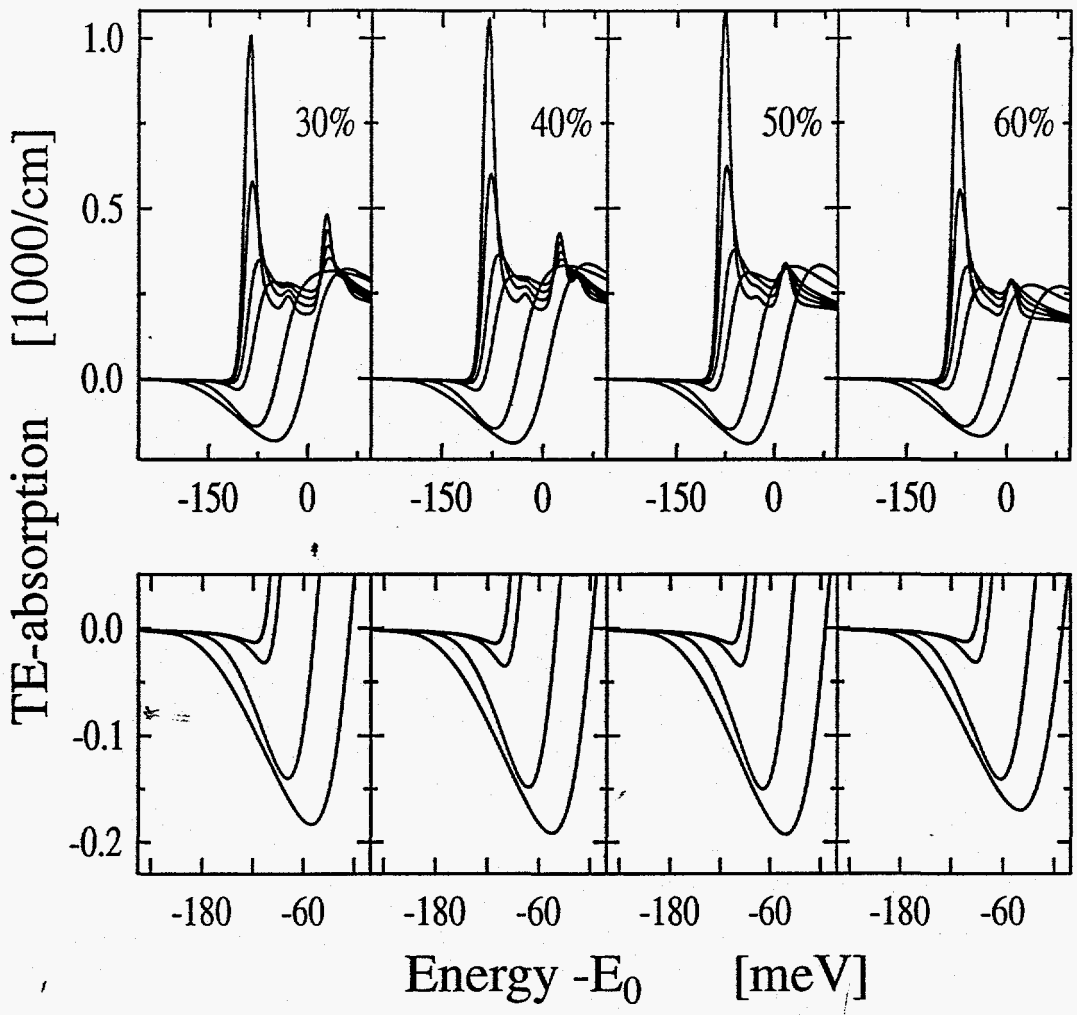
1.0
0.5
0.0
30%
40%
50%
60%
-150
0
-150
0
-150
0
-150
0
0.0
-0.1
-0.2
-180
-60
-180
-60
-180
-60
-180
-60
TE-absorption [1000/cm]
Energy -E0 [meV]

Fig 7

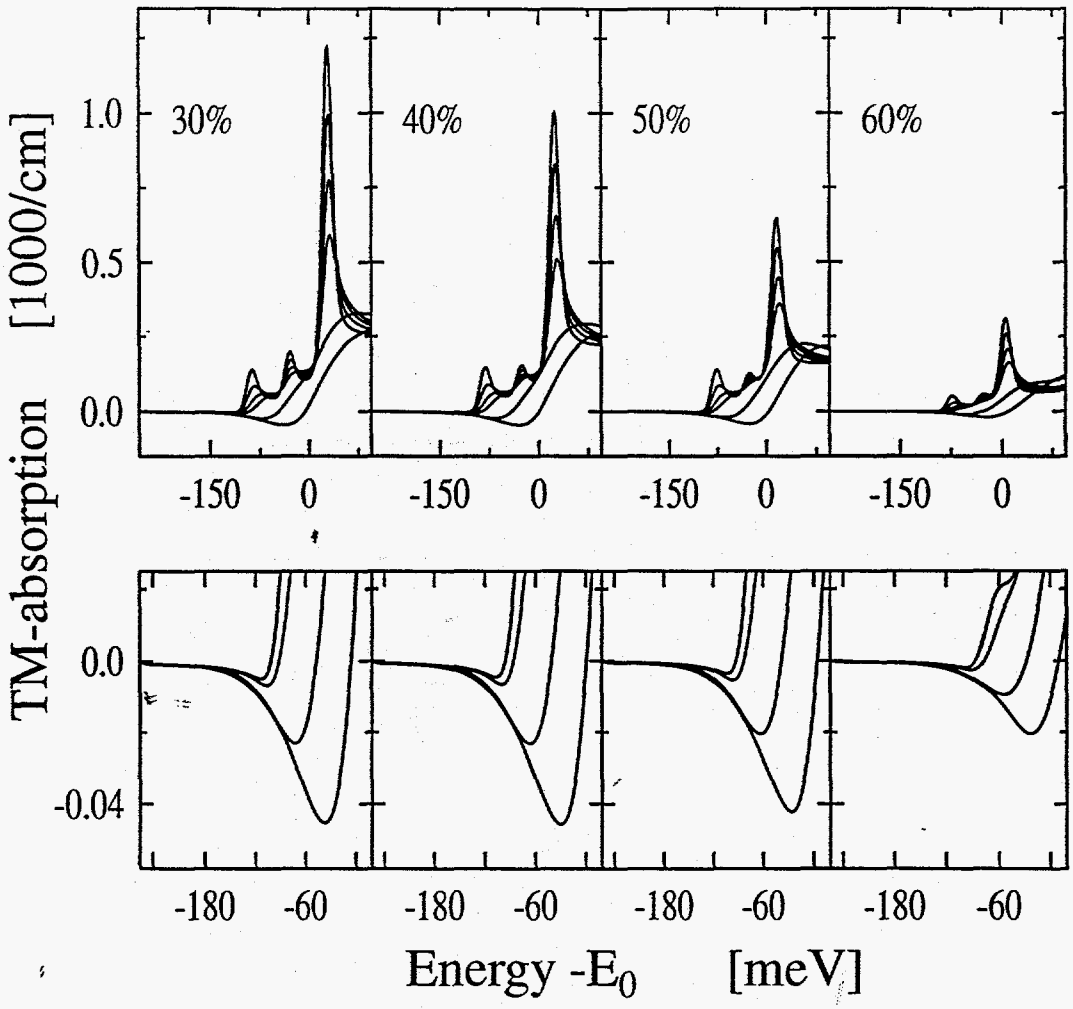
30%
40%
50%
60%
1.0
0.5
0.0
-150
0
0.0
-0.04
-180
-60
TM-absorption [1000/cm]
Energy -E0 [meV]

Fig8

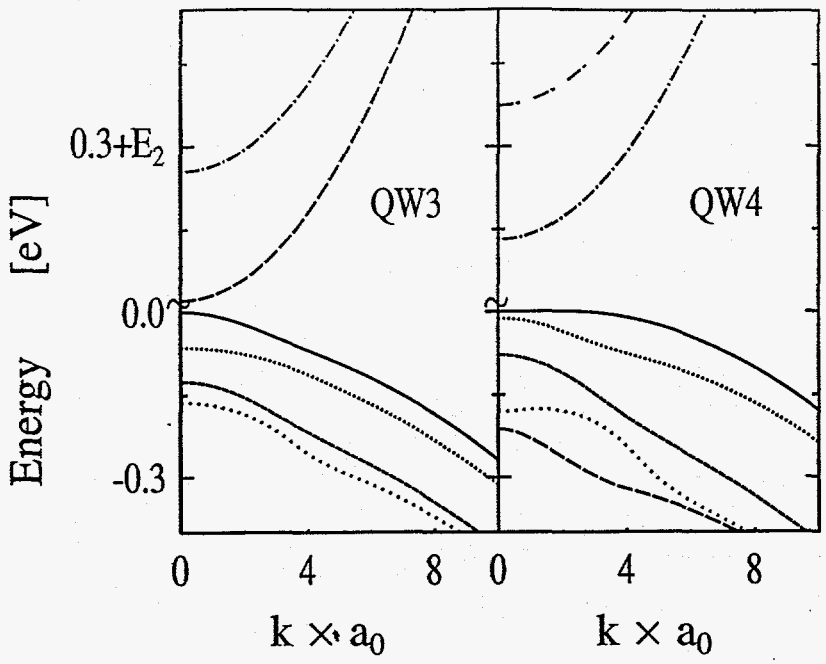

Fig 9

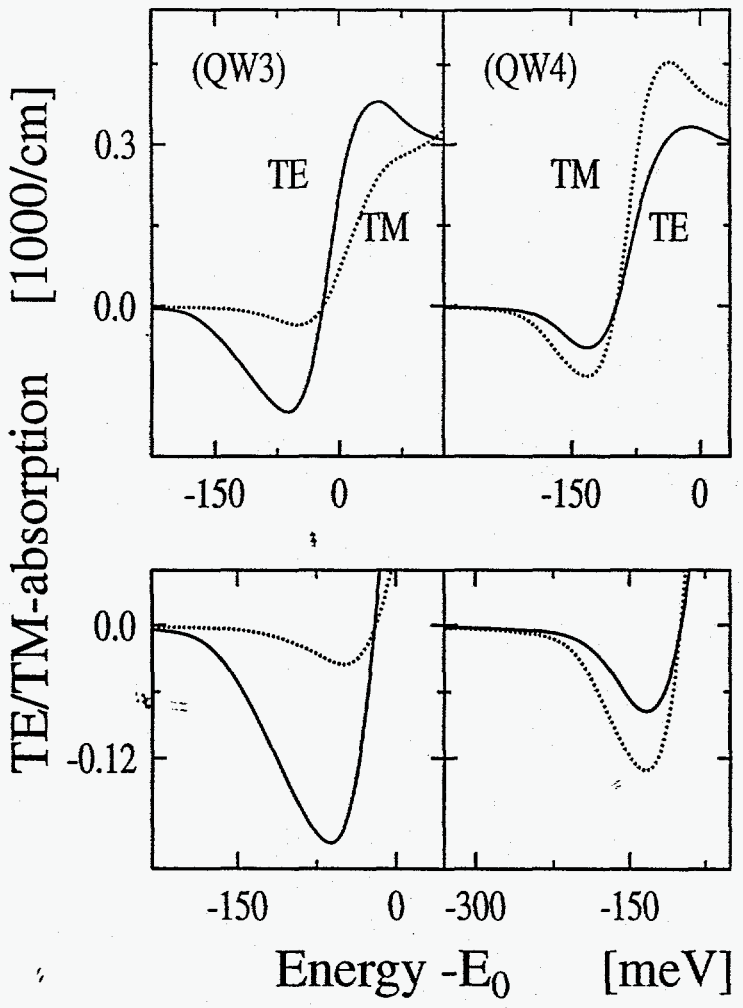
(QW3)
(QW4)
TE
TM
TM
TE
0.3
0.0
-0.12
-150
0
-300
TE/TM-absorption [1000/cm]
Energy -E0 [meV]

Fig 10

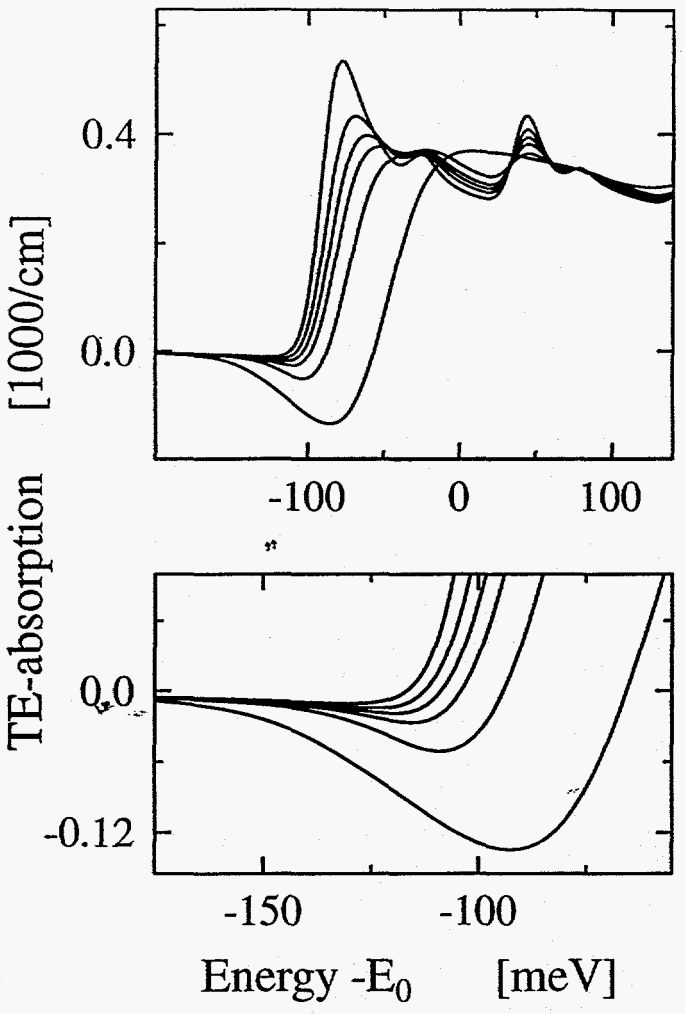
0.4
0.0
-100
0
100
TE-absorption [1000/cm]
0.0
-0.12
-150
-100
Energy -E0 [meV]

Fig 11